RSC Advances

PAPER

View Article Online
View Journal | View Issue

Cite this: *RSC Adv.*, 2024, **14**, 19512

Palladium(II), platinum(II), and silver(I) complexes with 3-acetylcoumarin benzoylhydrazone Schiff base: Synthesis, characterization, biomolecular interactions, cytotoxic activity, and computational studies†

Shadia A. Elsayed, * Islam M. Elnabky, Mohamed M. Aboelnga * and Ahmed M. El-Hendawy

New Pd(II) (**C1**), Pt(II) (**C2**), and Ag(I) (**C3**) complexes derived from 3-acetylcoumarin benzoylhydrazone (**HL**) Schiff base were synthesized and characterized by FTIR, ^{1}H NMR, UV-visible spectroscopies along with elemental analysis (C, H, N), magnetic, molar conductivity measurements, and DFT calculations. The obtained results suggested that the ligand had different behaviors in the complexes: mono-negative tridentate (**C1**) and neutral tridentate (**C2**) as an ONO-donor and neutral bidentate (**C3**) as an ON-donor. Quantum chemistry calculations were performed to validate the stability of the suggested geometries and indicated that all the complexes possess tetra-coordinated metal ions. The binding affinity of all the compounds toward calf thymus (ctDNA), yeast (tRNA), and bovine serum albumin (BSA) was evaluated by absorption/emission spectral titration studies, which revealed the intercalative binding to ctDNA and tRNA and static binding upon complex formation with BSA. Molecular insights into the binding affinity of the characterized complexes were provided through conducting molecular docking analysis. Moreover, the cytotoxic activity (*in vitro*) of the compounds was screened against human cancerous cell lines and a non-cancerous lung fibroblast (WI38) one using cis-platin as a reference drug. The IC_{50} and selective index (SI) values indicated the higher cytotoxic activity of all the metal complexes compared to their parent ligand. Among all the compounds, the complex **C2** showed the highest activity. These results confirmed the improvement of the anticancer activity of the ligand by incorporating the metal ions. In addition, flow cytometry results showed that complexes **C1** and **C2** induced cell cycle arrest at S and G1/S, respectively.

Received 12th April 2024
Accepted 2nd June 2024

DOI: 10.1039/d4ra02738h

rsc.li/rsc-advances

1. Introduction

Coumarins (2*H*-1-benzopyran-2-one) are a crucial class of oxygen-based heterocyclic compounds of natural origin and can be also found in synthetic medicinally active compounds.[1,2] They have been used in flavoring foods and in cosmetic products as a fragrant.[3] Coumarin-containing compounds have attracted considerable interest in biological applications including *in vitro*/*in vivo* anticancer,[4,5] antimicrobial, antioxidant, and anti-inflammatory activities.[1] In comparison to free coumarin-based ligands, the anticancer and antimicrobial activities have been enhanced by coordination with metal ions.[6–8] Recently, coumarin-derived Schiff bases along with associated metal complexes have been considered to be the most efficient classes of compounds that exhibit a wide range of biological activities.[7] It has been found that the **C3**-position of coumarin is an effective position that can improve the cytotoxic efficacy against several human cell lines.[9–11] In particular, 3-acetylcoumarin has demonstrated high reactivity to form remarkably stable Schiff base ligands such as hydrazone (ONO-donor ligands) and the synthesis of their metal complexes.[12]

On the other hand, hydrazone Schiff bases have also attracted considerable scientific attention owing to their unique structural and biological/pharmacological properties.[13–15] The keto–enol tautomerism of the hydrazone structure gives them the possibility to coordinate metal ions through azomethine nitrogen, or ketonic or enolic amide oxygen. Additionally, the coordination site from the substituent attached to the hydrazide amine group offers diverse coordination modes.[16–20] In fact, a series of hydrazide/hydrazine coumarin-based derivatives have been reported for their potential antitumor activity.[21] Moreover, hydrazone-based complexes were reported to improve the binding affinity to DNA, as well as the antitumor activity.[22,23] Therefore, the structural improvement of hydrazone/coumarin may lead

Chemistry Department, Faculty of Science, Damietta University, New Damietta, 34517, Egypt. E-mail: shadia.elsayed@du.edu.eg; mohamed-aboelnga@du.edu.eg

† Electronic supplementary information (ESI) available. See DOI: https://doi.org/10.1039/d4ra02738h

to an important category of compounds with utility for designing and developing new potential drugs.[24,25] Indeed, the literature is rich with numerous coumarin-derived complexes with therapeutic applications due to their anticancer, antimicrobial, and antioxidant effects and as enzyme inhibitors.[7,26] For instance, a series of 3-acetylcoumarin hydrazone Schiff base complexes containing nickel(II), cobalt(II), copper(II),[27] ruthenium(II), Rh(III), and Ir(III)[28] have been reported for their anticancer and antibacterial activities.

Based on the reported biological activities of coumarin, hydrazone Schiff bases, and their metal chelates, and also on a continuation of our research on acetylcoumarin and hydrazone Schiff bases,[29–31] we sought to develop novel metal complexes containing Pd(II), Pt(II), and Ag(I) based on 3-acetylcouamrin benzoylhydrazone Schiff base. Moreover, we evaluated their interaction with biomolecules (ctDNA, tRNA, and BSA), and in addition, their *in vitro* cytotoxic activity against human breast carcinoma (MCF7), cervical carcinoma (HeLa), and normal lung fibroblast (WI38) cell lines. Moreover, the cell death mechanism was elucidated by flow cytometry. Later, DFT calculations were performed to further support the proposed structures while molecular docking was carried out to provide deep insights into their interaction with BSA.

2. Experimental

2.1. Materials and equipment

Details on the materials and physical measurements are presented in the ESI materials (ESI,† Section 1.1).

2.2. Synthesis

2.2.1. Synthesis of 3-acetylcoumarin benzoyl hydrazone ligand (HL). A methanolic solution of 3-acetylcoumarine (0.94 g, 5 mmol) was added to benzyhydrazide (0.68 g, 5 mmol, 10 mL) in methanol in the presence of a few drops of glacial acetic acid. The mixture was refluxed for 3 h. The white product was filtered off, recrystallized from methanol, then dried in *vacuo*. Yield: 80%, m.p.: 158–160 °C. Elemental analysis for $C_{18}H_{14}N_2O_3$ (306.3): calcd (found): C, 70.58 (70.30); H, 4.61 (4.41); N, 9.15 (9.0). FTIR (KBr, cm^{-1}): ν (NH) 3192, ν(C=O)$_{lactone}$ 1721, ν(C=O)$_{hydrazone}$1664, ν(C=N) 1611, ν(N–N) 963 cm^{-1}. ^{1}H NMR (400 MHz, DMSO-d_6, δ, ppm): δ 10.85 (s, 1H, NH), δ 8.26 (s, 1H, H4), δ 7.88 (d, 2H, H6,9), δ 7.67 (t, 2H, H7,8), δ 7.53 (t, 2H, H16,18), δ 7.47 (d, 2H, H15,19), δ 7.41 (t, 1H, H17), δ 2.35 (s, 3H, H12). ^{13}C NMR (100 MHz, DMSO-d_6, δ, ppm): C(2) 159.7, C(3) 127.3, C(4) 142.4, C(5) 119.5, C(6) 116.5, C(7) 125.3, C(8) 133.5, C(9) 128.7, C(10) 151.6, C(11) 153.9, C(13) 128.3, C(14) 134.5, C(15,19) 130, C(16, 18) 129.7, C(17) 128.8, C(CH_3) 16.7. UV-vis (DMSO, 2.5 × 10^{-5} M): λ_{max} (nm) (ε, M^{-1} cm^{-1}): 232 (100 000), 336 (90 000).

2.2.2. Synthesis of [Pd(L)Cl] (C1) and [Pt(HL)Cl]Cl (C2). To a methanolic solution (10 mL) of the ligand **HL** (0.092 g, 0.3 mmol), an aqueous solution (2 mL) of K_2PdCl_4 (0.098 g, 0.3 mmol) or K_2PtCl_4 (0.125 g, 0.3 mmol) was added. The above solution was refluxed for 3 h. The precipitate was filtered off, washed with methanol followed by diethyl ether, and then dried.

[Pd(L)Cl] (**C1**): Yellow precipitate, yield: 75%, m.p.: 190–192 °C. Elemental analysis for $C_{18}H_{13}ClN_2O_3Pd$: calcd (found): C, 48.35 (48.03); H, 2.93 (2.80); N, 6.26 (6.14). FTIR (cm^{-1}): ν(C=O)$_{lactone}$ 1620, ν(C–O)$_{new}$ 1221, ν(C=N) 1589, ν(C=N)$_{new}$ 1554, ν(N–N) 975, ν(M–O) 575, ν (M–N) 442. ^{1}H NMR (400 MHz, DMSO-d_6, δ, ppm): δ 8.53 (s, 1H, H4), δ, 8.02, 7.85 (d, 2H, H6, 9), δ 7.66 (t, 2H, H7,8), δ 7.32 (t, 2H, H16,18), δ 7.42 (d, 2H, H15,19), δ 7.03 (t, 1H, H17), δ 2.66 (s, 3H, H12). UV-vis (DMSO, 2.5 × 10^{-5} M): λ_{max} (nm) (ε, M^{-1} cm^{-1}): 276 (127 000), 330 (52 000). Molar conductivity (10^{-3} M, DMSO), Λ_m = 2.0 Ω m^2 mol^{-1}.

[Pt(**HL**)Cl]Cl (**C2**): Orange precipitate, yield: 64%, m.p.: 200–202 °C. Elemental analysis for $C_{18}H_{14}Cl_2N_2O_3Pt$, calcd (found): 37.78 (37.86); H, 2.47 (2.39); N, 4.89 (4.77). FTIR (KBr, cm^{-1}): ν (NH) 3278, ν(C=O)$_{lactone}$ 1724, ν(C=O)$_{hydrazone}$ 1663, ν(C=N) 1575, ν(N–N) 1021, ν(M–O) 529, ν (M–N) 435. ^{1}H NMR (400 MHz, DMSO-d_6, δ, ppm): δ 10.72 (s, 1H, NH), δ 8.84 (s, 1H, H4), δ 8.13 (d, 2H, H6,9), δ 7.89 (t, 2H, H7,8), δ 7.60 (t, 2H, H16,18), δ 7.77 (d, 2H, H15,19), δ 7.50 (t, 1H, H17), δ 2.63 (s, 3H, H12). UV-vis (DMSO, 2.5 × 10^{-5} M): λ_{max} (nm) (ε, M^{-1} cm^{-1}): 276 (33 500), 327 (25 700). Molar conductivity (10^{-3} M, DMSO), Λ_m = 65 Ω m^2 mol^{-1}.

2.2.3. [Ag(HL)$_2$]NO$_3$ (C3). To a methanolic solution of the ligand **HL** (0.092 g, 0.3 mmol), an aqueous solution of $AgNO_3$ (0.05 g, 0.3 mmol) was added. The above solution was stirred under ambient conditions for 1 h. A grayish white precipitate formed was filtered, washed with methanol followed by diethyl ether, and then dried. Grayish white powder, yield: 70%, m.p.: 190–192 °C. Elemental analysis for $C_{36}H_{28}AgN_5O_9$: calcd (found): 55.26 (54.95); H, 3.61 (3.24); N, 8.95 (8.65). FTIR (KBr, cm^{-1}): ν (NH) 3277, ν(C=O)$_{lactone}$ 1698, ν(C=O)$_{hydrazone}$ 1664, ν(C=N) 1608, ν(N–N) 971, ν(M–O) 545, ν (M–N) 439. ^{1}H NMR (400 MHz, DMSO-d_6, δ, ppm): δ 11.05 (s, 1H, NH), δ 8.29 (s, 1H, H4), δ 7.90 (d, 2H, H6,9), δ 7.68 (t, 2H, H7,8), δ 7.56 (t, 2H, H16,18), δ 7.48 (d, 2H, H15,19), δ 7.42 (t, 1H, H17), δ 2.38 (s, 3H, H12). ^{13}C NMR (100 MHz, DMSO-d_6, δ, ppm): C(2) 161.6, C(3) 127.7, C(4) 142.5, C(5) 119.2, C(6) 116.7, C(7) 125.2, C(8) 133.3, C(9) 128.6, C(10) 151.6, C(11) 154.1, C(13), 128.7, C(14) 134.0, C(15,19) 129.7, C(16, 18) 129.5, C(17) 128.6, C(CH_3) 16.7. UV-vis (DMSO, 2.5 × 10^{-5} M): λ_{max} (nm) (ε, M^{-1} cm^{-1}): 226 (230 000), 332 (70 000). Molar conductivity (10^{-3} M, DMSO), Λ_m = 53 Ω m^2 mol^{-1}.

2.3. Solution stability

First, 50 μL (1.0 × 10^{-3} M) of the test compounds (in DMSO) was added to 1950 μL phosphate buffered saline (PBS, pH 7.2) in a UV-visible cuvette, until the final concentration reached 2.5 × 10^{-5} M. The electronic spectra were measured at set time intervals (0, 20, 40, 60 min, 24, and 48 h).

2.4. Biological studies

2.4.1. ctDNA, tRNA, and BSA interaction and MTT *in vitro* cytotoxic activity studies. Details on the experimental procedures are provided in the (ESI,† Section 1.2).

2.5. Theoretical calculations

2.5.1. DFT calculations. Density functional theory (DFT) calculations, as implemented in Gaussian 16 software, were utilized to obtain the most favorable structures for the three

studied complexes. The popular DFT functional B3LYP, which has been successfully used to study various metal-containing chemical systems, was used.[32–36] All the atoms were treated with the 6-311++G(3df,3pd) basis set except the metal ion that was represented based on the effective core potential (ECP) and LANL2DZ basis set. To further validate the identity of the obtained stable geometries as stationary points, frequency calculations at the optimization level of theory were performed on the optimized complexes, and no imaginary frequency was detected. Gaussian 16 utilities were also used to obtain the frontier molecular orbitals (FMOs) for the studied molecules, which helps to better explain their chemical reactivity. The determined FMOs, including the highest occupied molecular orbitals (HOMOs) and lowest unoccupied molecular orbitals (LUMOs), were visualized using Gaussian view.

2.5.2. Docking methodology. To provide atomistic insights into the binding between the characterized complexes and the albumin protein, molecular docking calculations were performed using Autodock4 tools.[37,38] The structure of bovine serum albumin was retrieved from PDB ID: 6QS9[39] and refined by deleting the crystalized water molecules, assigning hydrogens to the standard amino acids, and adjusting the Kollman charges. Then, the default settings available in Autodock tools were utilized to assign the overall forcefield for the standard amino acids and then the protein was converted into pdbqt format. The optimized geometries for the complexes obtained from our DFT calculations were used as ligands for the docking analysis and were converted into pdbqt format while the charges were computed by the Gasteiger model. To accurately identify the most favorable binding pocket, MGL tools were used for blind docking by constructing a grid box that spread over the entire protein obtained from ref. 37. The genetic Algorithm protocol was selected to perform our molecular docking and the number of runs was set to 20 runs. The energetically favorable binding modes that lead to the highest binding scores were chosen for deeper structural analysis. Chimera software was then used to obtain detailed figures for the bound protein ligands.[40]

3. Results and discussion

3.1. Synthesis

The ligand 3-acetylcomarin benzoylhydrazone Schiff base (**HL**) and its complexes (**C1**)–(**C3**) were prepared and characterized, as shown in the Experimental section (Section 2.2). The analytical data revealed that the molar ratio (M : L) of the complexes was 1 : 1 metal-to-ligand except for [Ag(**HL**)$_2$], which seemed to have a 1 : 2 ratio. All the complexes were completely soluble in DMF, and DMSO but sparingly soluble in common organic solvents (methanol, ethanol, CH_2Cl_2, CH_3CN, *etc.*). The molar conductance values of 10^{-3} M in DMSO suggested the neutrality of the [Pd(L)Cl] complex (**C1**) (Λ_M = 2.0 Ω^{-1} cm^2 mol^{-1}), while the 1 : 1 electrolytic nature[41] of the other complexes Pt(II) (**C2**) ((Λ_M = 65 Ω^{-1} cm^2 mol^{-1}) and Ag(I) (**C3**) were in the range of Λ_M = 53 Ω^{-1} cm^2 mol^{-1}). The analytical data suggest that the complexes **C1–C3** were four coordinates, as indicated in Fig. 1.

3.2. Characterization

3.2.1. Vibrational spectra. The FTIR spectral bands of 3-acetylcoumarin benzoylhydrazone Schiff base (**HL**) and its complexes **C1–C3** (ESI, Fig S1a–d†) were assigned as detailed in the Experimental section (Section 2.2) and Table S1.† The FTIR spectrum of the **HL** ligand displayed strong bands at 3192 and 1664 cm^{-1} due to the stretching vibrations of ν(NH) and carbonyl oxygen ν(C=O) of the hydrazone moiety, respectively, suggesting that the ligand displayed an amido keto-form in its solid state (Scheme 1a). In addition, the strong bands that appeared at 1721 cm^{-1} were attributed to ν(C=O) of the lactone ring. The strong band at 1611 cm^{-1} was due to azomethine ν(C=N) stretching vibrations.[42] Moreover, bands assigned to amide(II), amide(III), and ν(N–N) were observed at 1536, 1273, and 963 cm^{-1}, respectively.[43,44]

Generally, the azomethine stretching band ν(C=N) was shifted to a lower frequency, suggesting the participation of azomethine-*N* in coordination with the metal center; however, a diversity of coordination modes was shown by the complexes. For example, in complex [Pd(L)Cl] (**C1**) (Fig. 1), the **HL** ligand

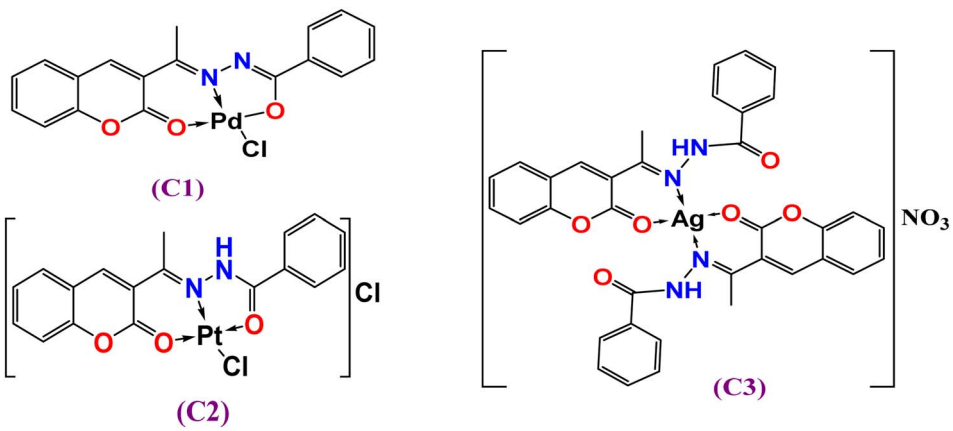

Fig. 1 Suggested structures of complexes C1–C3.

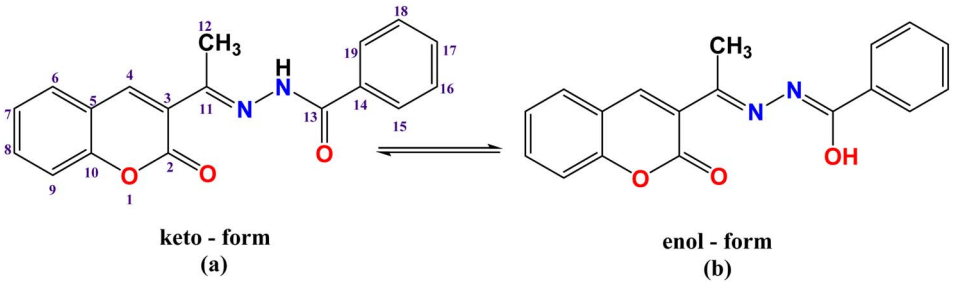

Scheme 1 (a) Keto-form, and (b) enol form of the HL ligand with the atom labeling scheme.

behaved in a mono-negative tridentate (ONO) manner. This is illustrated by the lower frequency shifts of both the azomethine (C=N) and lactone (C=O) groups. Also, there was a disappearance of the ν(NH) and ν(C=O)$_{hydrazinic}$ through coordination (deprotonation after enolization (Scheme 1b), as supported by the appearance of a new ν(C=N) group[45] near 1589 cm^{-1}, besides the shift of the ν(N–N) band to a higher frequency by 7–58 cm^{-1}. This, in turn, indicated that the bonding occurred through enolate oxygen, accordingly, and new ν(C–O) bands were obtained at 1221 and 1213, respectively. This assumes that the ligand behaves as a mono-negative tridentate using azomethine-*N*, carbonyl-*O*, and lactone-*O*.[45,46] In the FTIR spectrum of [Pt(**HL**)Cl]Cl (**C2**), the presence of ν(NH) and ν(C=O)$_{hydrazinic}$ bands, and the lower frequency shifts of azomethine (C=N) and lactone (C=O) indicate that the coordination took place in a neutral tridentate (ONO) manner. In the FTIR spectrum of [Ag(**HL**)$_2$]NO$_3$ (**C3**), the ν(NH) band was shifted to a higher frequency (3277 cm^{-1}), while the ν(HC=N) and lactone-O bands were shifted to lower frequencies; hence the ligand coordinated in a neutral bidentate manner (ON-donor). In addition, the strong absorption near 1365 cm^{-1} was attributed to the stretching vibration of ν(NO$_3$).[47] For all the complexes, new medium bands were observed at 435–449 and 529–575 cm^{-1}, assigned to ν(M–N) and ν(M–O), respectively.[47]

3.2.2. NMR spectra. ^{1}H NMR spectra of all the compounds (ESI, Fig. S2a–d†) were recorded in DMSO-d$_6$ and assigned in the Experimental section (Section 2.2) and Table S2.† The atom labeling scheme of the ligand is presented in Scheme 1. The ^{1}H NMR spectrum of the free ligand (**HL**) (Fig. S2a†) showed singlet signals at δ 10.85, 8.26, and 2.35 ppm, assignable to NH, H(4), and methyl protons H(12), respectively, while the doublets observed at δ 7.88, 7.47 ppm were attributed to four protons of H6,9 and H15,19. In addition, triplets appeared at δ 7.67, 7.53, and 7.41 ppm and were assigned to H7,8, H16,18, and H17, respectively. In the spectrum of [Pd(L)Cl] (**C1**) complex (Fig. S2b†), the absence of the –NH signal proved that **HL** binds to the metal centers in its enolic form[48,49] (Scheme 1). Conversely, the presence of the –NH signal in the ^{1}H NMR spectra of both [Pt(**HL**)Cl]Cl (**C2**) (Fig. S2c†) and [Ag(**HL**)$_2$]NO$_3$ (**C3**) (Fig. S2d†) indicates that **HL** coordinated through its keto-form, confirming the data proposed by the FTIR spectra. Also, all the other protons adjacent to the coordination sites were shifted upfield to some extent.[50,51] Generally, for silver(I) complexes, the spectra are not so different when compared to the free ligand, particularly, when the ligand coordinates as a neutral species, or the d^{10} electronic configuration of Ag(I) ion.[52]

The ^{13}C NMR of **HL** (Fig. S3a and Table S3†) showed signals at 153.9 and 159.7 and 16.7 ppm assigned to C(11) and C(2) and the methyl carbon CH$_3$ group, respectively similar to an earlier reported ligand.[45] These signals were slightly shifted downfield in the spectrum of the Ag(I) complex (Fig. S3b†). This downfield shift by ~2 ppm indicated the contribution of lactone carbonyl oxygen in the coordination. Moreover, the upfield shift of azomethine-C indicates that the ligand coordinated as an ON-donor through lactone carbonyl oxygen, and azomethine nitrogen. Noteworthily, the ^{1}H and ^{13}C of the silver complex exhibited very little shift in comparison to the parent ligand. This was anticipated due to the coordination of the ligand in its neutral mode and the Ag(I) ion's d^{10} electronic configuration.

3.2.3. Electronic spectra. The UV-visible spectra of the ligand (**HL**) and its complexes **C1–C3** (10^{-5} M) (Fig. 2) were recorded in DMSO solvent (Experimental section, Section 2.3, Table S4†). The UV-visible spectrum of the ligand showed bands at 232 and 336 nm attributed to the (π–π*) transition of phenyl rings, and (n–π*) transition of –C=N– and –C=O– moieties,[53,54] respectively. The electronic spectra of the complexes exhibited a hypsochromic (blue-shift) of these transition bands, along with changes in the absorbance intensity, which were due to the coordination to the center of the metal ions.[55,56]

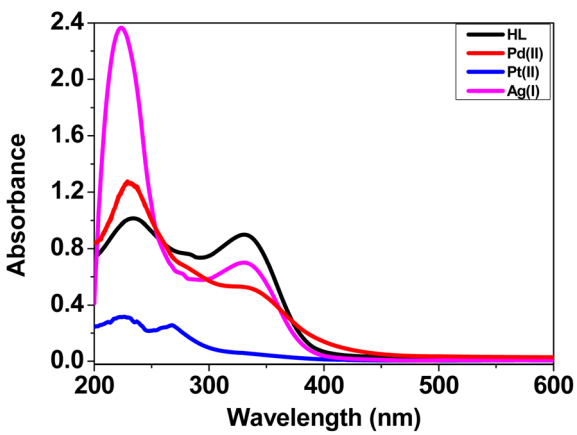

Fig. 2 UV-visible spectra of HL and complexes C1–C3 (10^{-5} M) in DMSO.

3.2.4. Solution stability. The solution stability study of the metal complex is a very important step to decide the reactivity of a metal complex in biological applications. The solution stability of the compounds was studied in an aqueous solution (PBS, pH 7.2) using UV-visible spectroscopy analysis at set time intervals (0, 30 min, 1 h, 1.5 h, 2 h, 3 h, 1 day, and 2 days) as shown in Fig. S4.† It was observed that the ligand showed insignificant changes up to the first 3 h then suffered hydrolysis in the aqueous media through the next 24 h. No distinctive changes were observed for the complexes (**C1–C3**) during the first 6 h. These results indicated the stability of these complexes under physiological conditions in buffer–DMSO solution.[57] After 24 h, a slight decrease in absorption intensity of the complexes (**C1** and **C3**) was observed, which may be attributed to the solvent exchange ($DMSO/H_2O$) with chloride and nitrate ions, respectively; however complex (**C2**) showed insignificant changes during the 48 h test.[58,59]

3.2.5. DFT calculations. The geometries for the synthesized complexes were characterized in both vacuum and a water medium. Notably, both Pt(II) and Pd(II) metal ions adopted an identical square planner geometry with a tri-coordinate **HL** ligand while the chloride ion ligand fulfilled the tetra-coordinated sphere, Fig. 3. The coordinating distances for both geometries are quite similar with an average distance of 2.0 Å where N or O centers are the coordinating atoms. Meanwhile, the M···Cl chelating distance was found to be the longest, with an average distance of 2.30 Å. Meanwhile, the obtained Ag(I) coordination geometry resulting from the 2 : 1 ratio was subtly different with a double ligation from each **HL** molecule. Its coordination distances were slightly longer than the corresponding ones in Pt(II) and Pd(II) complexes with an average distance of 2.47 Å. Interestingly, the calculated geometries for the three complexes were in accordance with the proposal from the experimental results.

Moreover, the most stable geometries for the studied complexes were fully optimized in aqueous medium using a similar functional and basis set combination to further validate their stability in solution. A comparison between the obtained geometries from these later calculations demonstrated there were insignificant changes in both their overall structure and the ligation distances, which agreed well with the experimental observations, Fig. 3. To better explain the chemical reactivity of the three complexes, the energy gap parameter, ΔE, was determined for each complex from the difference between the energy of the highest occupied molecular orbital (E_{HOMO}) and the energy of the lowest unoccupied molecular orbital (E_{LUMO}). In fact, the ΔE value is a stronger procurer for the chemical reactivity of the compounds and the smaller the gap the higher the reactivity of the complex. According to our calculations, the determined energy gap values were found to be 0.0902, 0.0974, and 0.135 au for the Pt(II)-, Pd(II)-, and Ag(I)-containing complexes. Moreover, the softness quantum chemical parameter ($\sigma = 1/\Delta E$) was calculated and the obtained order for their values was Pt(II) > Pd(II) > Ag(I), with the Pt(II)-containing complex demonstrating the highest value. Therefore, the obtained order of the reactivity from our calculation from both the ΔE and σ values agreed well with the experimental observations.

The HOMO and LUMO were also displayed to better represent the delocalization and localization behavior of the electrons over the characterized complexes, Fig. 3. It was also noted that the HOMO of the Pt(II)- and Pd(II)-containing complexes behaved similarly and mainly localized over both the metal centers and the ligated chloride ions. It is also important to

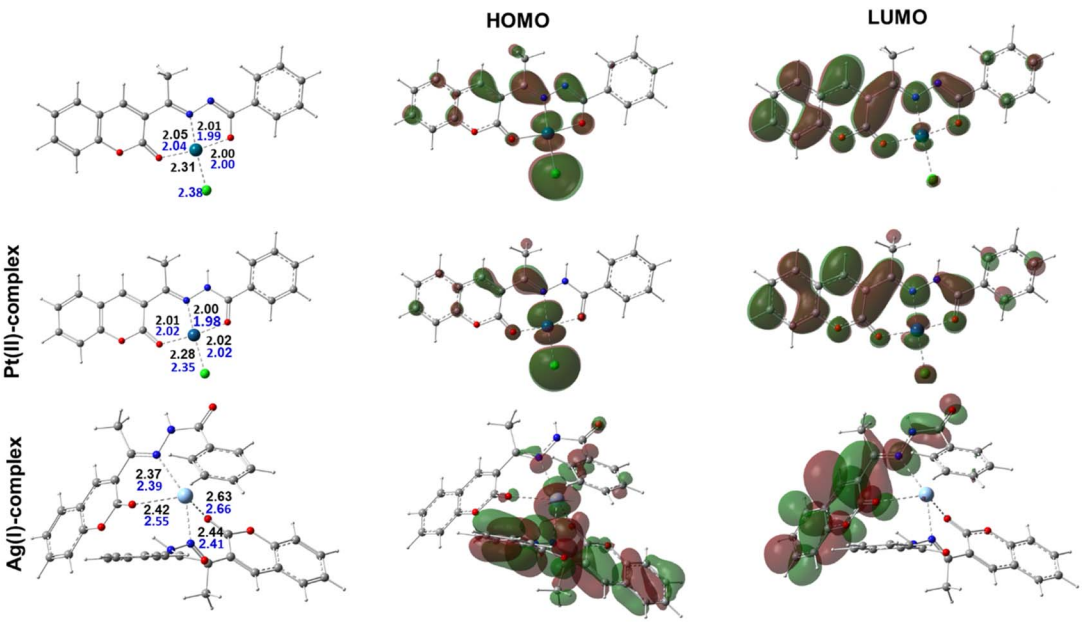

Fig. 3 Optimized molecular geometries for the three complexes representing the synthesized complexes together with selected bond distances in (Å) for optimization in gas (blue) and aqueous media (black), and their respective HOMOs and LUMOs.

point out that a minor contribution from the ligated atom in the Pd(II) complex in the HOMO was also noticed. For the Ag(I) complex, however, in addition to the localization over the metal center, a significant participation of the aromatic motifs for one of the chelated ligands was observed. Meanwhile, the delocalization of the LUMO also showed some similarity among the three complexes in being distributed over conjugated π-systems of the aromatic rings in the ligand. Overall, this later observation could suggest that the geometry around the metal center together with the conjugated bonds over the aromatic motifs in the ligand are key players in the activity of the studied complexes.

4. Biological applications

4.1. ctDNA and tRNA interaction studies

Transition metal complexes have a very important function in metallodrug design. They can interact with DNA/RNA *via* different binding modes: intercalation (insertion), groove binding (major or minor), or electrostatic interaction.[60] The intercalative binding is considered the most important one,[61] because the molecules are inserted among the base pairs of the DNA double helix, forming π–π stacking interactions that induce elongation and unwinding of the DNA double helix due to the separation of the base pairs to accommodate the drug, and consequently, the DNA binding is responsible for various biological activities; for example, antitumor, antimicrobial, antiviral, anti-inflammatory, and antimalarial properties.[62,63] In this section, we evaluated the ctDNA/tRNA binding affinity to the test compounds using both absorption and emission spectroscopies.

4.1.1. Absorption studies. The absorption spectral changes of the **HL** and its complexes (**C1–C3**) upon the addition of variable concentrations of ctDNA or tRNA to the test compound were monitored using UV-visible spectroscopy in Tris–HCl buffer (pH 7.2). The electronic spectra were first recorded for the free compound. The addition of different concentrations of the biomolecules may result in a slight red/blue-shift in the wavelength along with a hypochromic (a decrease in absorption intensity) or hyperchromic (increase in absorption intensity) shift.[64] In our compounds (Fig. 4), the free ligand (**HL**) showed a hypochromic shift at $\lambda_{max} = 314$ nm (intraligand π–π* transition), while the complexes (**C1–C3**) showed hypochromic shifts at 320, 329, and 319 nm, respectively (Fig. 4); this change suggests that the ligand and its complexes behaved with the same binding mode (intercalation). Also, the presence of the isosbestic point (change from hypochromism to hyperchromism) at 293 nm (**HL**), 319 nm (**C2**), and 295 nm (**C3**) indicated that there were only two absorbing species (free nucleic acid and nucleic acid–complex) with the same absorbance in equilibrium in the solution media.[65]

The presence of the aromatic chromophore existing in the ligand aided the interaction of the compounds with the CT DNA bases *via* non-covalent π–π* stacking interactions, wherein the

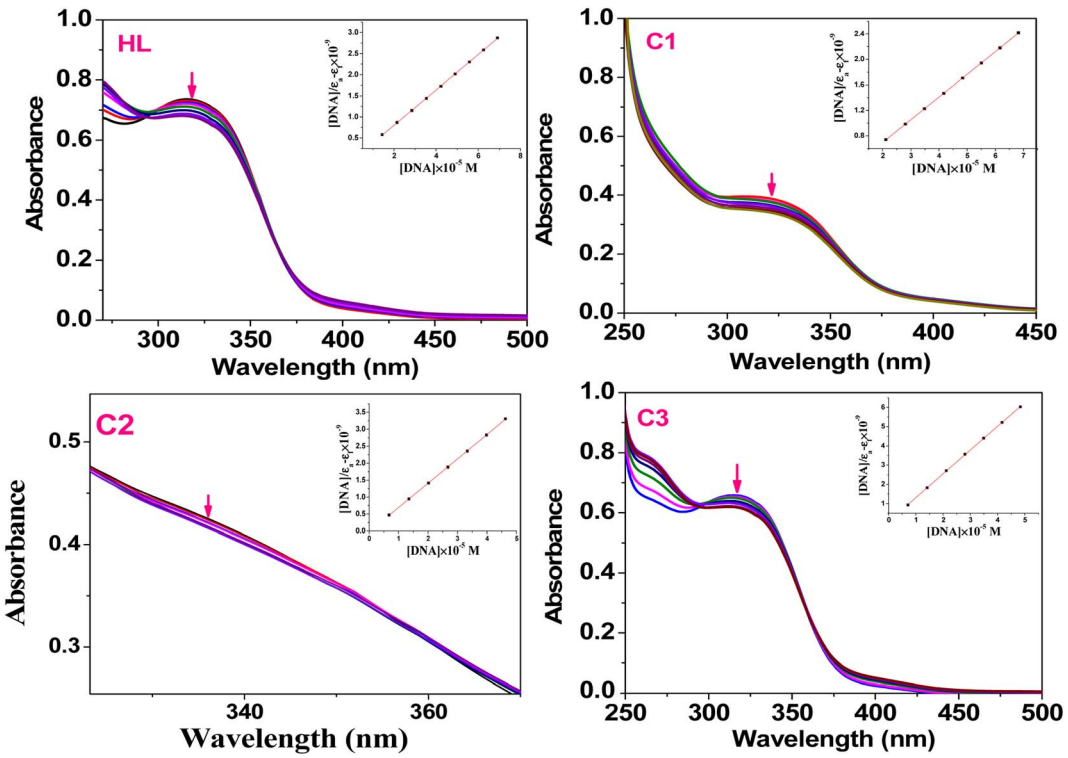

Fig. 4 Absorption spectra of the ligand (HL) and C1–C3 complexes (50 μM) in the presence of different concentrations of ct DNA (5–50 μM) in Tris–HCl buffer (pH 7.2); (inset): linear plot of ([DNA]/ε_a–ε_f) *vs.* [DNA].

Table 1 Binding constant data (K_b, K_{sv}) along with % hypochromism (% H) obtained from the interaction study of the compounds with ctDNA and tRNA

		Absorption spectroscopy				Emission spectroscopy (at λ_{em} = 580 nm)			
		(K_b), × 10^6		% H*		(K_{sv}),×10^4		% H	
Compd	λ_{max}	ctDNA	tRNA	ctDNA	tRNA	ctDNA	tRNA	ctDNA	tRNA
HL	314	1.10	1.36	8.35	7.20	0.34	1.19	32.4	26.1
(**C1**)	320	4.71	10.3	12.7	8.67	4.91	7.52	55.4	61.5
(**C2**)	329	2.58	8.96	10.4	7.60	1.42	4.51	54.2	48.8
(**C3**)	319	1.22	1.51	6.81	6.66	0.52	1.6	50.1	26.9

π*-orbital of the ligand in the complexes could couple with the π-orbital of the DNA base pairs. The binding constants (K_b) was determined using the Wolfe–Shimer eqn (1):[66]

$$\frac{[DNA/RNA]}{(\varepsilon_a - \varepsilon_f)} = \frac{[DNA/RNA]}{(\varepsilon_a - \varepsilon_f)} + \frac{1}{K_b(\varepsilon_a - \varepsilon_f)} \quad (1)$$

where [DNA] and [RNA] are the molar concentrations of ctDNA and tRNA, respectively, $\varepsilon_a = A_{obs}/[compound]$ is the apparent absorption coefficient, and ε_f and ε_b correspond to the extinction coefficients of the free and bound compound. The K_b (slope–intercept ratio) values were obtained from the plot of [DNA]/(ε_a–ε_f) against [DNA]. The K_b values of the ligand and its metal complexes were found to be in the order of 10^6 M^{-1}. The binding constants of the metal complexes followed the order (**C1**) > (**C2**) > (**C3**) > (**HL**), revealing a relatively high binding constant of the Pd(II) complex (**C1**) compared to the free ligand and other complexes, as shown in Table 1. This conclusion indicates that complexation enhanced the binding ability of the metal complexes with the nucleic acid (ctDNA and tRNA). The UV-visible absorption spectra of complexes with tRNA are presented in the ESI materials (Fig. S5†).

4.1.2. Emission spectroscopy. As the compounds lack fluorescent properties, we used the ethidium bromide assay (EB) to further confirm the intercalation of the small molecules to ctDNA and tRNA, whereby EB increases the fluorescence intensity (at λ_{em} = 580 nm) when bound to ctDNA or tRNA after intercalating between their base pairs. At this wavelength, the fluorescence quenching spectra (Fig. 5) of the complexes (**C1–C3**) and their free ligand (**HL**) showed that the compounds were able to displace EB from DNA-EB/RNA-EB adducts (the reduction in the emission intensity indicates the binding of the compound with ctDNA or tRNA due to the formation of a non-fluorescent DNA/RNA-complex) and confirmed that ligands/complexes had intercalated onto nucleic acid base pairs.

The quenching constant (K_{sv}) values (Table 1) were determined by the Stern–Volmer eqn (2):[67]

$$I_o/I = 1 + K_{SV}[Q] \quad (2)$$

where I_o and I are the emission intensities of the test compound in the absence and presence of ctDNA/ tRNA , respectively, K_{SV} is the Stern–Volmer constant, and [Q] is the concentration of the compound.

4.2. Bovine serum albumin (BSA) interaction studies

The protein interaction with metal complexes has become an interesting research area, where anticancer drugs are mostly administrated *via* intravenous injection into the bloodstream, where they are bound to plasma protein.[68] The drug–protein binding strength displays a significant role in its accessibility to diffuse from the blood to the target.[69] In the following section, we evaluated the binding affinity of BSA protein (human serum albumin analog) by employing absorption and emission measurements.

4.2.1. Absorption studies. Absorption spectroscopy is one of the most helpful techniques to examine the structural changes and quenching type of BSA by drug molecules. The absorption titrations of **HL** and its complexes (**C1–C3**) with BSA in PBS at physiological pH 7.2 are shown in Fig. 6. Generally, the interaction should occur in a static or dynamic mode. In the static mechanism, a non-fluorescent BSA-complex was formed in the ground state before excitation of any electrons and resulted in changes in the absorption profile. However, in the dynamic mechanism (collisional), the fluorophore interacts with the quencher during the temporary existence of the excited state. Additionally, the dynamic mechanism affects only the excited state, with no alternation on the absorption spectrum.[70] In the case of our complexes, with the increasing amounts of the **HL** ligand or its complexes, the absorption intensity increased (with 11.9–40.74% hyperchromism) together with a blue-shift of 2–4 nm in the range of 260–450 nm. This is an indication of the formation of the BSA–complex in the ground state *via* a static interaction. These results also showed that the structural changes may be attributed to the non-covalent interactions; for instance, electrostatic and hydrogen bonding interactions between the **HL** ligand and the complexes with the BSA.[71,72] The binding constants were evaluated by eqn (3)[73,74] and are tabulated in Table 2.

$$1/(A_o - A) = 1/A_o + 1/(K \times A_o \times C_Q) \quad (3)$$

where A_o is the absorbance of unbound BSA, A is the absorbance of bound BSA (after the addition of different concentrations of the test compounds), respectively, K is the binding constant, and C_Q is the compound concentration. The K value can be obtained from the linear plot of $1/(A_o - A)$ against 1/[comp.] from the intercept-to-slope ratio.

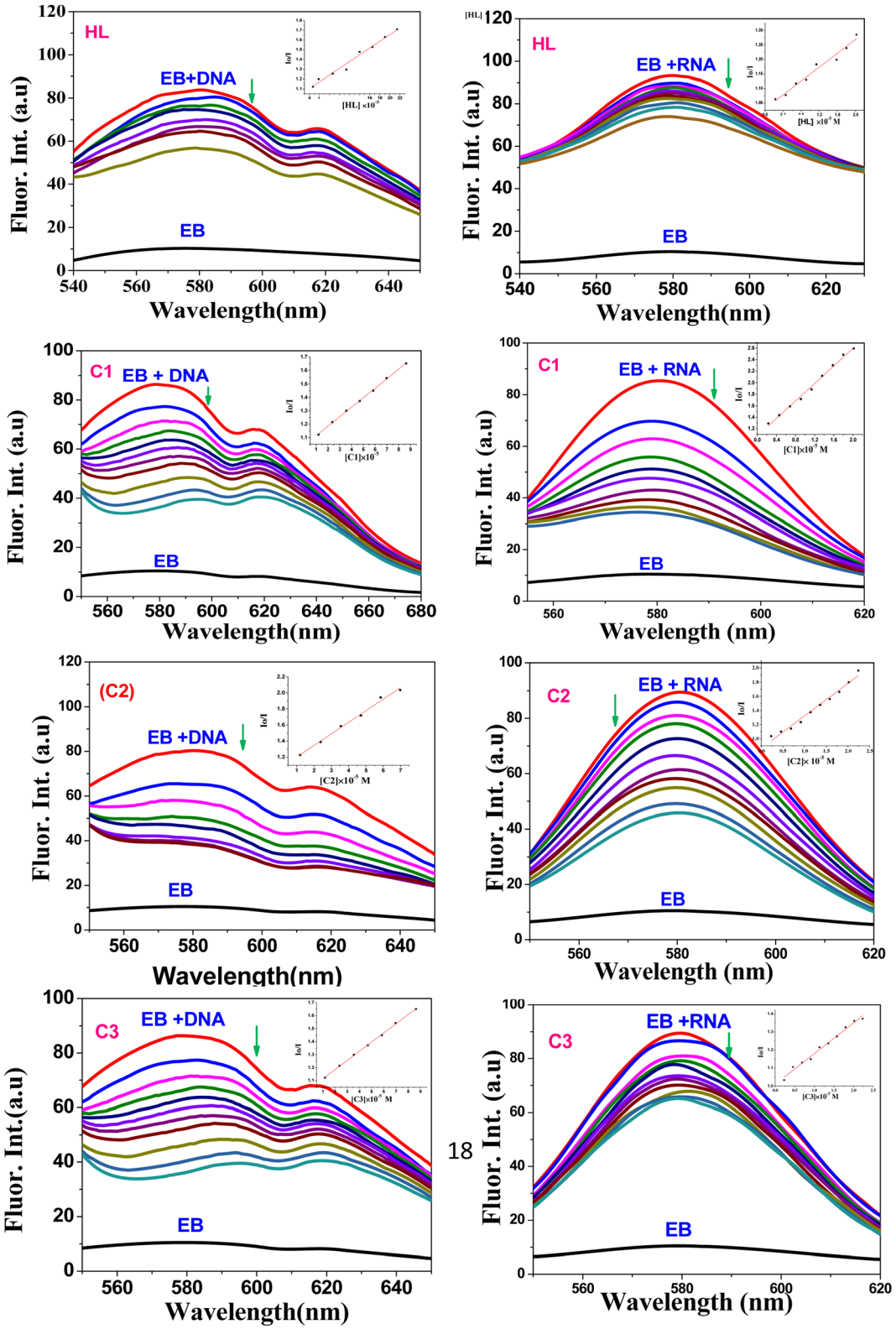

Fig. 5 Fluorescence quenching spectra of EB-ctDNA/EB-tRNA adduct in the presence of HL and C1–C3 compounds; [EB] = 5 μM; Left: [DNA] = 50 μM, [*Q*] = 10–200 μM, Rright: [RNA] = 50 μM, [*Q*] = 10–200 μM; (inset): plot of I_o/I *vs.* [*Q*].

4.2.2. Emission studies. Emission spectroscopy is one of the most efficient tools to study the quenching mechanism, and binding interaction mode the compounds with BSA.[75,76] The BSA solution is excited at 278 nm due to the presence of tyrosine and tryptophan residues in proteins, emitting a strong peak at 345 nm. Fig. 7 shows that the emission intensity (*I*) of BSA

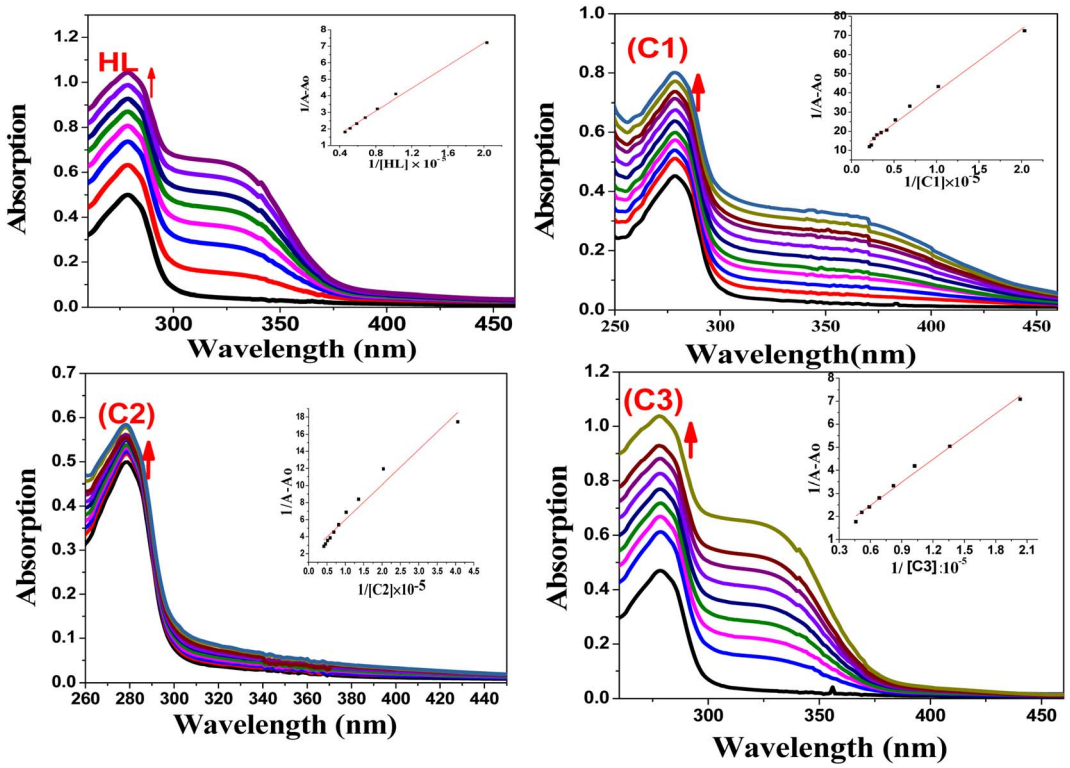

Fig. 6 Electronic absorption spectra of BSA (50 μM) in the presence of different concentrations of **HL** and **C1–C3** complexes (0–50 μM) pH 7.2 (Tris–HCl buffer); (inset): linear plot of $1/[(A - A_o)]$ *vs.* 1/[compound].

Table 2 Binding (K_b) and quenching constant (K_q) data and the number of binding sites (n) of BSA interaction with the titled compounds[a]

Absorption spectroscopy $\lambda_{max} = 278$ nm			Emission spectroscopy $\lambda_{max} = 345$ nm				
Compound	(K_b), $\times 10^4$	% hyper	% hypo	(K_{sv}), $\times 10^4$	(K_q), $\times 10^{12}$	(K_b)	n
HL	1.0	39.03	27.18	2.33	2.33	8.9×10^3	0.93
(**C1**)	4.6	36.05	69.44	5.68	5.68	4.0×10^5	1.61
(**C2**)	2.5	11.90	42.63	5.39	5.39	3.9×10^4	1.03
(**C3**)	1.52	40.74	35.69	4.98	4.98	2.6×10^4	0.92

[a] The observed BSA binding constant (K) values for all the compounds are presented in (2). It was found that the **C1** complex exhibited the highest binding strength with BSA in the order of **C1** > **C2** > **C3** > **HL**.

decreases upon addition of different amounts upon complexes (**C1–C3**) or the ligand **HL** with a slight shift in the peak position (~2 nm). The results indicate that the BSA intrinsic fluorescence decreases due to the formation of a non-fluorescent complex with BSA. The Stern–Volmer eqn (2)[77,78] mentioned above ($I_o/I = 1 + K_{sv}[Q]$) was used to evaluate the fluorescence quenching constant. The Stern–Volmer quenching constant (K_{sv}) was obtained from the slope of the plot of I_o/I *vs.* [compound]. The quenching rate constant, K_q was determined using eqn (4)

$$K_q = K_{sv}/\tau_o \quad (4)$$

where K_q is the quenching rate constant, and τ_0 is the average lifetime of protein in absence of the quencher and it is taken as 10^{-8} s for BSA.[79]

The maximum collision quenching constant (K_q) for biomacromolecules with various quenchers is 10^{10} M^{-1} s^{-1}.[80] In our study, the resulting K_q values were 0.5–6.1 × 10^{12} M^{-1} s^{-1}, which were higher than 10^{10} M^{-1} s^{-1}, confirming the static quenching (rather than dynamic) because of the formation of a ground state complex between BSA and the quenchers,[81] which confirmed the data obtained from the absorption spectra.

The static binding constant (K_b) and the number of binding sites can be further calculated from the modified Stern–Volmer eqn (5):[69,82,83]

$$\log[(I_o - I)/I] = \log K_b + n \log[Q] \quad (5)$$

K_b and n can be determined from a plot of $\log[(I_o - I)/I]$ *vs.* $\log[Q]$ (Fig. 8), specifically from the slope and intercept values, respectively. The n values for the serum albumin-complex were around the 1.0 value (Table 2), indicating the presence of single binding site in BSA for the compound. Here, we can conclude

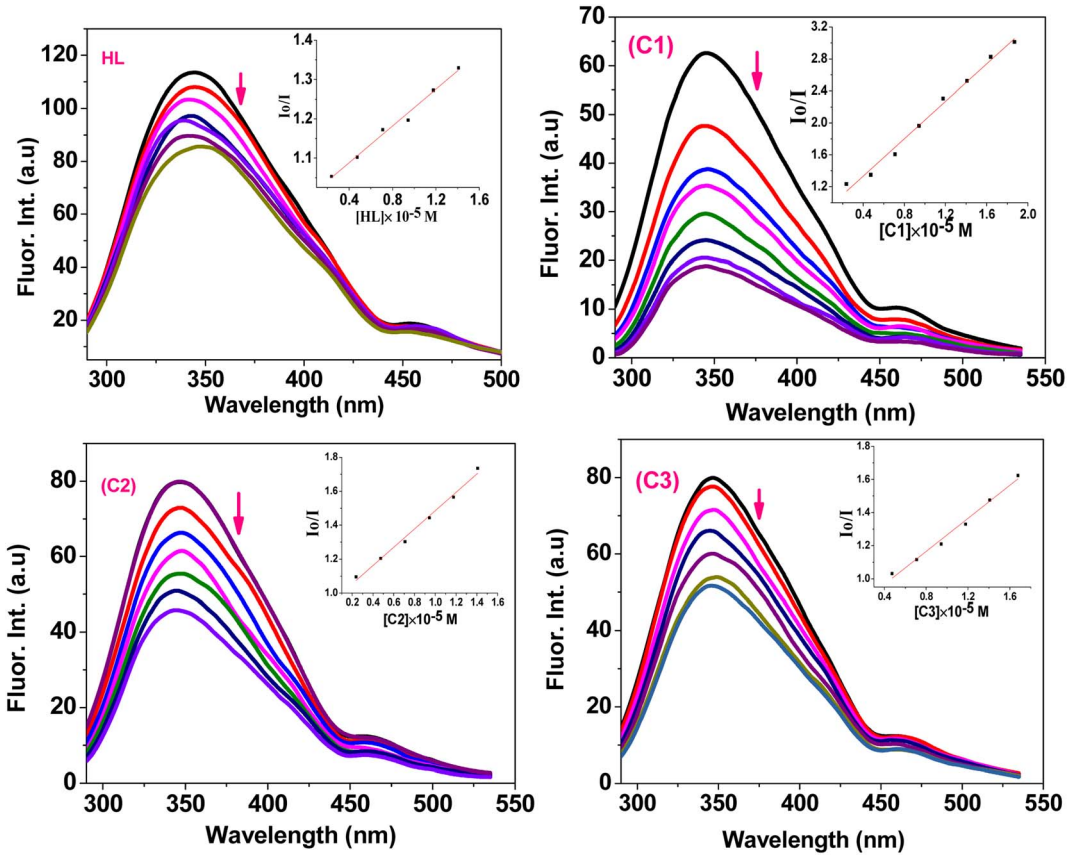

Fig. 7 Emission spectra of BSA (50 μM) upon addition of different concentrations of HL and complexes (C1–C3) (0–50 μM) in DMSO/PBS solution. (Inset): plots of I_o/I *vs.* [compound].

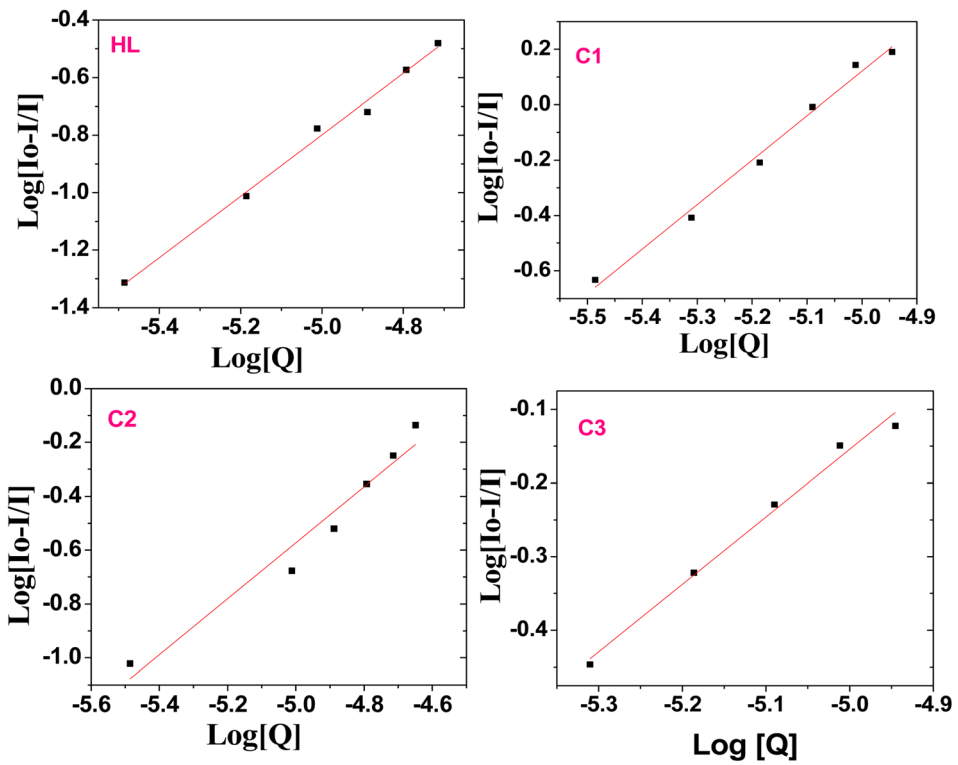

Fig. 8 Plot of $\log((I_o - I)/I)$ *versus* log[*Q*] after adding various amounts of the ligand (HL) and complexes C1–C3 to BSA.

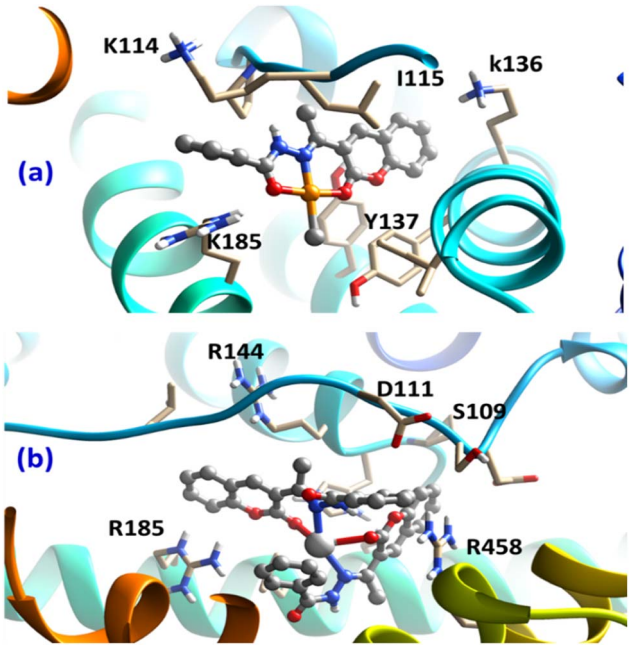

Fig. 9 Obtained bound complexes for (a) Pt(II) and (b) Ag(I) complexes with the BSA target. The key amino acids participating in the interactions are highlighted.

that the binding ability of the compounds to the biomolecules would be very useful in drug design, where it can enhance the drug stability and toxicity during chemotherapeutic processes.

4.2.3. Molecular docking results. Our docking calculations for both the Pt(II)- and Ag(I)-containing complexes on the targeted BSA protein revealed the affinity of our complexes to the biomolecules. In particular, both complexes showed high binding ability with binding scores of −8.62 and −7.97 kJ mol^{-1} for the Pt(II) and Ag(I) complexes, respectively, Fig. 9.

Despite binding to distinct locations over the BSA target, both ligands were involved in different types of interaction with the surrounding amino acids of the protein. Most importantly, the cation–π interaction between cationic amino acids, arginine and lysine in particular, with the aromatic domains of the chelating **HL** were the most dominant interaction. Interestingly, the subtle difference in the obtained binding scores of the two complexes suggested the binding preference of Pt(II)-containing compound over the Ag(I) one, in accordance with the experimental binding results. These obtained findings from the docking analysis further support the validity of the synthesized complexes to act as potential drugs.

4.3. *In vitro* anticancer activity

The *in vitro* cytotoxic effects of **HL** and its complexes (**C1–C3**) were evaluated by the colorimetric MTT assay against two human cancer cell lines, namely hormone-dependent breast (MCF7) and cervical (HeLa), in addition to a non-cancerous one, namely the human lung fibroblast (WI38), using cis-platin as a standard drug with exposure times of 24 and 48 h. The results of this study (Table 3, Fig. 10 and 11) showed that all the complexes possessed higher antitumor activity than their parent ligand based on the IC_{50} and selective index (SI) values. The data revealed that the HeLa cell lines were more sensitive to the complexes than the MCF7 cell lines, as observed from the IC_{50} and SI values (Table 3). Moreover, all the complexes were found to be more toxic than cis-platin in the HeLa and MCF7 cell lines.

The cytotoxicity and the mechanism of metal complexes mainly depend on their geometry, oxidation state of the metal ion, and redox potential.[87–89] According to the IC_{50} values, the Pt(II) complex (**C2**) showed the highest cytotoxic activity (*i.e.*, a lower IC_{50}, specifically, $IC_{50} = 8.12 \pm 0.7$ for HeLa, and 12.33 ± 0.9 for MCF7), which may be due to the cationic nature of the Pt(II)[86] rather than the neutral Pd(II) complex, where $IC_{50} = 10.77 \pm 0.9$ for HeLa and 19.47 ± 1.5 for MCF7. It has been reported that Pd(II) complexes are less stable than Pt(II) ones, because they have a higher aquation rate.[90–92] However, the SI values of the Pd(II) complex(**C1**) (SI = 5.31 for HeLa and 2.94 for MC7) were higher than those of the Pt(II) complex (**C2**) (SI = 3.63 for HeLa and 2.39 for MCF7), indicating that the Pd(II) complex was

Table 3 *In vitro* cytotoxic activity (IC_{50}) and selective indices (SI) values of the ligand and its complexes (**C1–C3**) against WI38, HeLa, and MCF7 cell lines for 24 and 48 h

	In vitro cytotoxicity IC_{50} (μM) and selective indices values				
Compound no.	WI38	HeLa	SI	MCF7	SI
24 h					
HL	71.11 ± 3.4	61.62 ± 3.1	1.15	40.83 ± 2.6	1.74
(C1)	57.22 ± 2.8	10.77 ± 0.9	5.31	19.47 ± 1.5	2.94
(C2)	29.51 ± 2.2	8.12 ± 0.7	3.63	12.33 ± 0.9	2.39
(C3)	75.42 ± 3.6	39.08 ± 2.5	1.93	58.79 ± 2.9	1.28
Std.	25.56 ± 2.1	34.58 ± 1.63	0.74	31.2 ± 1.8 (ref. 84)	0.82
48 h					
HL	74.98 ± 3.5	47.57 ± 2.9	1.57	36.78 ± 2.4	2.03
(C1)	45.24 ± 2.7	9.79 ± 0.8	4.62	13.40 ± 0.9	3.37
(C2)	31.28 ± 2.2	6.31 ± 0.4	4.95	8.61 ± 0.6	3.63
(C3)	63.60 ± 3.3	32.52 ± 2.3	1.95	54.04 ± 3.0	1.66
Cisplatin	26.68 ± 2.2	67.6 ± 2.0 (ref. 85)	0.39	72.38 ± 0.1 (ref. 86)	0.36

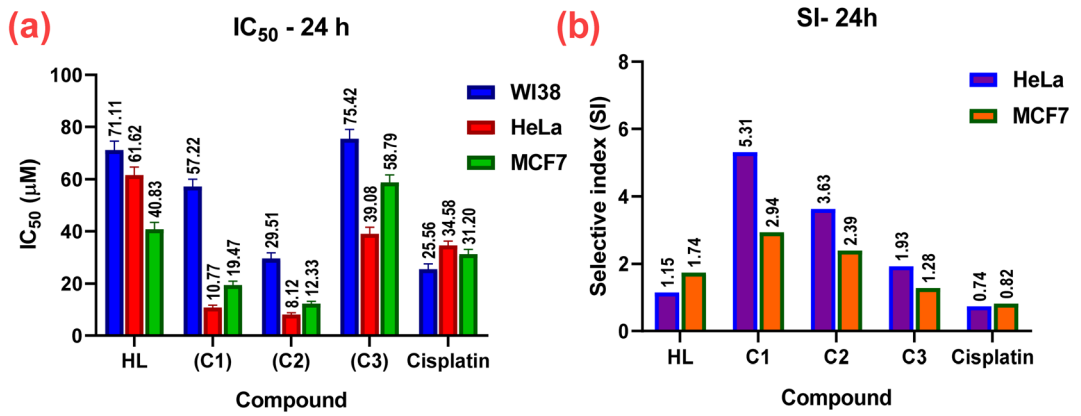

Fig. 10 *In vitro* cytotoxicity; (a) IC_{50} and (b) SI values of the complexes (C1–C3), their parent ligand (HL), and cis-platin (standard) against normal WI38, and cancerous HeLa, and MCF7 human cell lines at 24 h.

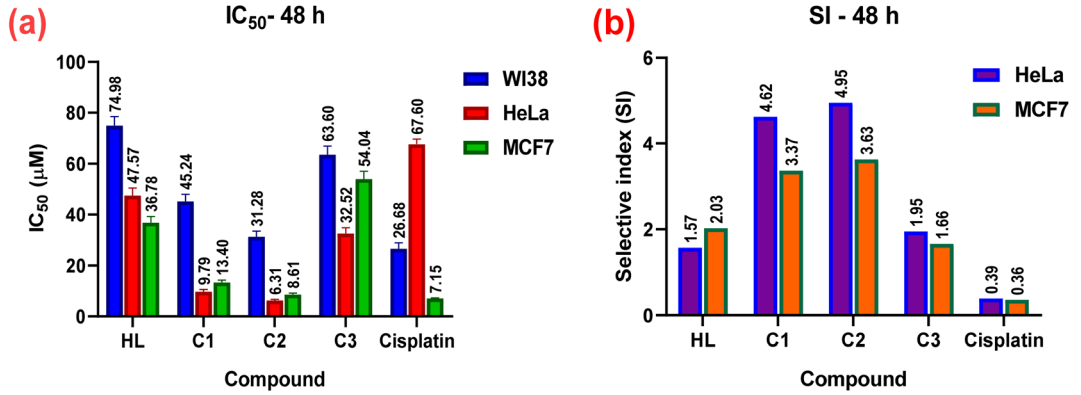

Fig. 11 *In vitro* cytotoxicity; (a) IC_{50} and (b) SI values of the complexes (C1–C3), their parent ligand (HL), and cis-platin against normal WI38, and cancerous HeLa, and MCF7 human cell lines at 48 h.

more selective and safe for both cell lines. The silver(I) complex had less effect, which may be attributed to the steric hindrance[90,93,94] from the introduction of two ligands around the Ag(I) ion (or reduced electrophilicity), which retards the intercalation of the silver(I) complex with DNA (as shown from the binding study, mentioned before), and hence decreased its cytotoxic activity (higher IC_{50}) for both cell lines, as shown in Table 3. It also demonstrated higher selectivity toward both cell lines. Among all the complexes, complex **C1** showed the highest selectivity for the tumorous HeLa and MCF7 cells, so, it will be selected in the future for further investigations for better understanding the mechanism of action.

4.3.1. Cell cycle arrest by C1 and C2. Based on the binding affinity and cytotoxicity results, the complexes **C1** and **C2** were subsequently selected for further investigation on HeLa cells. The cell cycle distribution of HeLa cells was investigated by flow cytometry after being treated with the IC_{50} concentrations of either complex **C1** or **C2** (10.77 and 8.12 μM, respectively) for 24 h, as shown in Fig. 12. Cell cycle progression analysis showed that treatment of HeLa cells with complex **C1** resulted in a significant decrease in the number of cells in the G0/G1 phase (46.52% compared to the control cells' 52.17%, $p = 0.003$). The G2/M phase did not show any significant change (18.07% compared to the control cells' 20.3%, $p = 0.155$). These findings suggest that the treatment with complex **C1** prohibited the entrance of HeLa cells into a new cycle. Furthermore, there was a notable increase in the S-phase population percentage (35.41% compared to the control cells' 27.53%, $p = 0.027$) in HeLa cells treated with complex **C1**, indicating cell cycle arrest at the S phase. This arrest may be attributed to the binding of complex **C1** with the DNA, which hindered the replication of DNA and the production of new cells.[95] On the other hand, the cell cycle analysis for HeLa cells treated with complex **C2** showed no significant changes in either the G0/G1 or S phases compared to the untreated HeLa cells. Conversely, there was a significant reduction in the G2/M phase (20.3% compared to the control cells' 15.96%, $p = 0.042$). These data suggest the cells were prevented from entering mitotic cell division.

4.3.2. Induction of cell death mode by complexes C1 and C2. The induction of cell death was studied by flow cytometry using the Annexin V/propidium iodide (PI) method to distinguish between live and dead cells in four quadrants, namely Q1 (viable cells, lower left), Q2 (early apoptotic cells, lower right), Q3 (late apoptotic cells, upper right), and Q4 (necrotic cells,

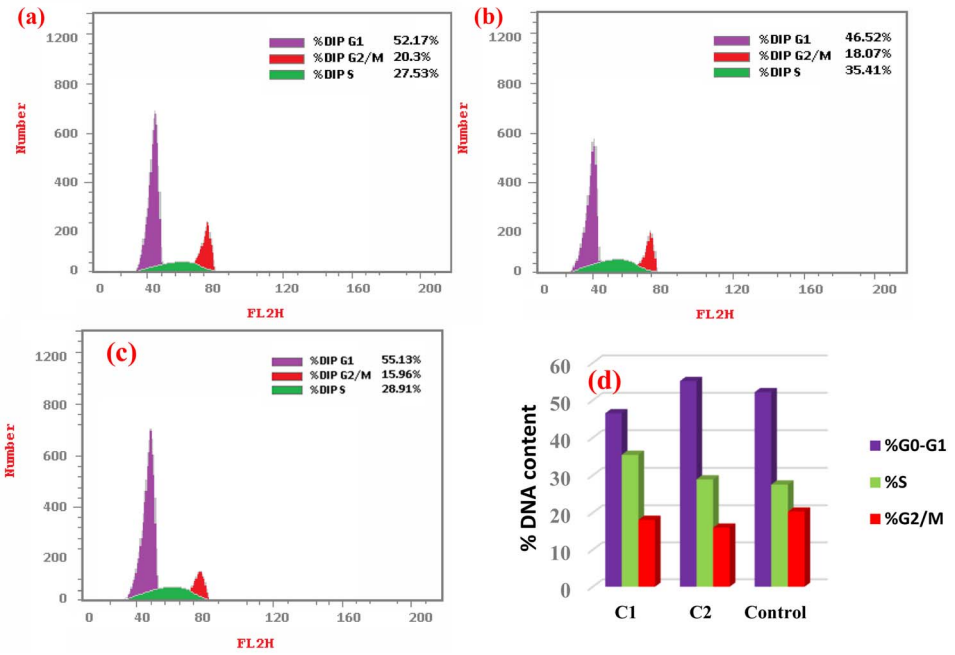

Fig. 12 Cell cycle phases (%) in (a) control (untreated HeLa cells), (b) HeLa treated with complex **C1**, (c) HeLa treated with complex **C2** at IC_{50} concentrations for 24 h. (d) Plot presenting the cell cycle distribution (%).

upper left), as shown in Fig. 13. After 24 h incubation of HeLa cells with either complexes **C1** or **C2** and by investigating their IC_{50}, it was observed that the proportion of both early and late apoptotic cells was significantly increased for both complexes compared to untreated HeLa cells as the control, *i.e.*, 23-fold and 49-fold for complex **C1**, and 42.7-fold and 89.6-fold for

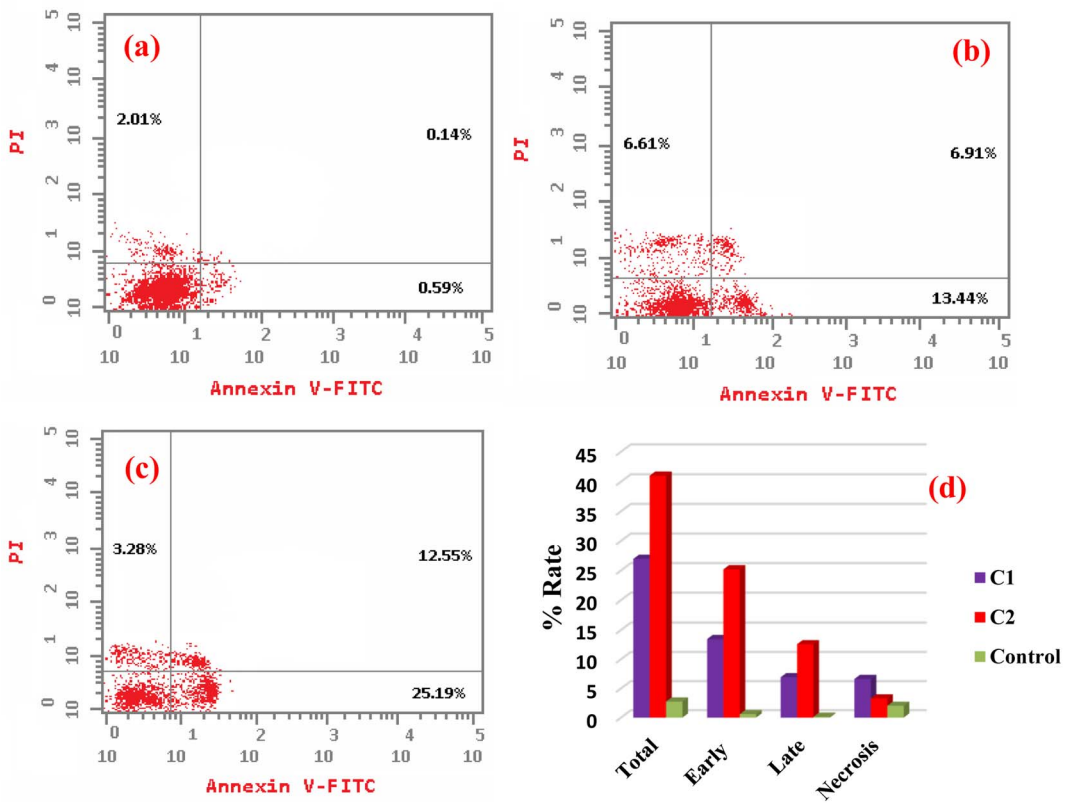

Fig. 13 Apoptotic/necrotic dot plots of (a) untreated HeLa cells, (b) cells treated with complex **C1**, (c) cells treated with complex **C2** for 24 h. (d) Plot presenting the total, early, and late apoptosis, and necrosis percentage.

complex **C1**. Compared to the necrotic cells, there were no significant changes (3.3-fold for **C1**, and 1.6-fold for **C2**). The data suggest that these metal complexes demonstrating the cell death *via* early and late apoptosis.[96]

5. Conclusions

In this study, three new metal complexes of Pd(II), Pt(II), and Ag(I) (**C1–C3**) derived from 3-acetylcoumarin benzoylhydrazone (**HL**) were prepared and characterized by elemental analysis, spectroscopic techniques, and DFT calculations. The analytical data revealed that the ligand acted as an ONO-donor forming square planar geometries for the Pd(II) and Pt(II) complexes. The **HL** was coordinated to Pd(II) centers in its deprotonated form, while in the case of Pt(II) it was coordinated in its neutral form. However, in the Ag(I) complex it was coordinated as a neutral ON-donor. The binding affinity of all the compounds toward ctDNA, yeast tRNA, and BSA was assessed by electronic and fluorescence spectra. All the compounds showed the intercalative mode of binding, and the data revealed that the Pd(II) and Pt(II) complexes showed the highest binding strength (K_b) to these molecules. This latter observation was further emphasized by our molecular docking calculations, which provided a higher binding score for the Pt(II) complex than Ag(I). The key interaction responsible for the tight interaction between the targeted BSA and the two complexes was mainly a cation–pi interaction, where the cationic residues arginine and lysine represent the cationic motifs. Furthermore, the cytotoxic activity (*in vitro*) of the compounds was estimated against a non-cancerous WI38 and cancerous HeLa and MCF7 cell lines using the MTT assay for 24 and 48 h. The data showed that the Pd(II) and Pt(II) complexes had the highest toxicity based on the IC_{50} and selective indices (SI) values, consistent with the biomolecular interaction studies. Furthermore, the results from flow cytometry demonstrated that complexes **C1** and **C2** caused cell cycle arrest at S and G1/S, respectively.

Abbreviations

B3LYP	Becke, 3-parameter, Lee–Yang–Parr
BSA	Bovine serum albumin
ctDNA	Calf thymus deoxyribonucleic acid
DFT	Density functional theory
DMSO	Dimethylsulfoxide
EB	Ethidium bromide
FTIR	Fourier-transform infrared
HeLa	Cervical carcinoma cell line
HOMO	Highest unoccupied molecular orbital
K_b	Intrinsic binding constant
K_{sv}	Stern–Volmer constant
K_q	Quenching binding constant
LANL2DZ	Los Alamos National Laboratory 2 double-zeta
LMCT	Ligand-to-metal charge transfer
LUMO	Lowest unoccupied molecular orbital
MCF7	Mammary gland breast cancer
MGL	Machine graded lumber
MTT	3-(4,5-Dimethylthiazol-2-yl)-2,5-diphenyltetrazoliumbromide
NA	Nucleic acid
NMR	Nuclear magnetic resonance
PBS	Phosphate buffered saline
PI	Propidium iodide
SI	Selective index
tRNA	Transfer ribonucleic acid
Tris–HCl	Tris(hydroxymethyl)aminomethane hydrochloride
UV-vis	Ultraviolet-visible spectroscopy
WI38	Human lung fibroblast cell line
ε_a	Apparent extinction coefficients
ε_b	Extinction coefficients bound compound
ε_f	Extinction coefficients of the free complex

Data availability

The data that support the findings of this study are available from the corresponding author upon reasonable request.

Author contributions

Shadia A. Elsayed: supervision, conceptualization, formal analysis, software, resources, visualization, methodology, software, validation, writing – original draft. Islam M. Elnabky: software, validation, methodology. Ahmed M. El-Hendawy: supervision, conceptualization, visualization, writing – review & editing. Mohamed M. Aboelnga: supervision, visualization, data curation, software, formal analysis, calculation, writing – original draft.

Conflicts of interest

There are no conflicts of interest to declare.

Acknowledgements

We acknowledge the Ministry of Higher Education of Egypt for CIQAP (CP3-016-MAN) project, and the Academy of Scientific Research and Technology (ASRT), Egypt, under initiatives of science up capacity building (Grant No. 6389) for research equipment funds.

References

1 T. Pereira, D. Franco, F. Vitorio and A. Kummerle, *Curr. Top. Med. Chem.*, 2018, **18**, 124–148.
2 O. Halter and H. Plenio, *Eur. J. Inorg. Chem.*, 2018, **2018**, 2935–2943.
3 P. Manojkumar, T. K. Ravi and G. Gopalakrishnan, *Acta Pharm.*, 2009, **59**, 159–168.
4 M. P. Sathisha, U. N. Shetti, V. K. Revankar and K. S. R. Pai, *Eur. J. Med. Chem.*, 2008, **43**, 2338–2346.
5 M. Mladenović, N. Vuković, S. Sukdolak and S. Solujić, *Molecules*, 2010, **15**, 4294–4308.
6 M. P. Sathisha, U. N. Shetti, V. K. Revankar and K. S. R. Pai, *Eur. J. Inorg. Chem.*, 2008, **43**, 2338–2346.

7 S. A. Patil, V. Kandathil, A. Sobha, S. B. Somappa, M. R. Feldman, A. Bugarin and S. A. Patil, *Molecules*, 2022, **27**, 5220.
8 S. Balcioğlu, M. Karataş, B. Ates, B. Alici and I. Ozdemir, *Bioorg. Med. Chem. Lett.*, 2020, **30**, 126805.
9 C. Ranjan Sahoo, J. Sahoo, M. Mahapatra, D. Lenka, P. Kumar Sahu, B. Dehury, R. Nath Padhy and S. Kumar Paidesetty, *Arab. J. Chem.*, 2021, **14**, 102922.
10 B. S. Creaven, E. Czeglédi, M. Devereux, É. A. Enyedy, A. Foltyn-Arfa Kia, D. Karcz, A. Kellett, S. McClean, N. V. Nagy, A. Noble, A. Rockenbauer, T. Szabó-Plánka and M. Walsh, *Dalton Trans.*, 2010, **39**, 10854–10865.
11 A. Pangal, J. Shaikh and E. Khan, *Int. J. Pharmaceut. Sci. Rev. Res.*, 2017, **42**, 161–168.
12 S. Aslkhademi, N. Noshiranzadeh, M. S. Sadjadi, K. Mehrani and N. Farhadyar, *Polyhedron*, 2019, **160**, 115–122.
13 R. Kaplánek, M. Havlík, B. Dolenský, J. Rak, P. Džubák, P. Konečný, M. Hajdúch, J. Králová and V. Král, *Bioorg. Med. Chem.*, 2015, **23**, 1651–1659.
14 S. Omidi and A. Kakanejadifard, *RSC Adv.*, 2020, **10**, 30186–30202.
15 G. Le Goff and J. Ouazzani, *Bioorg. Med. Chem.*, 2014, **22**, 6529–6544.
16 Y. Li, Z. Yang, M. Zhou, J. He, X. Wang, Y. Wu and Z. Wang, *J. Mol. Struct.*, 2017, **1130**, 818–828.
17 P. K. Suganthy, R. N. Prabhu and V. S. Sridevi, *Polyhedron*, 2015, **88**, 57–62.
18 R. N. Prabhu and R. Ramesh, *J. Organomet. Chem.*, 2012, **718**, 43–51.
19 H. H. Monfared, M. Vahedpour, M. M. Yeganeh, M. Ghorbanloo, P. Mayer and C. Janiak, *Dalton Trans.*, 2011, **40**, 1286–1294.
20 S. A. Elsayed, I. M. Elnabky, A. di Biase and A. M. El-Hendawy, *Appl. Organomet. Chem.*, 2022, **36**, e6481.
21 T. Nasr, S. Bondock and M. Youns, *Eur. J. Med. Chem.*, 2014, **76**, 539–548.
22 M. Mishra, K. Tiwari, S. Shukla, R. Mishra and V. P. Singh, *Spectrochim. Acta, Part A*, 2014, **132**, 452–464.
23 I. Ali, K. Saleem, D. Wesselinova and A. Haque, *Med. Chem. Res.*, 2013, **22**, 1386–1398.
24 P. P. Netalkar, A. Kamath, S. P. Netalkar and V. K. Revankar, *Spectrochim. Acta, Part A*, 2012, **97**, 762–770.
25 Y.-h. Li, B.-d. Wang and Z.-y. Yang, *Spectrochim. Acta, Part A*, 2007, **67**, 395–401.
26 Ł. Balewski, S. Szulta, A. Jalińska and A. Kornicka, *Front. Chem.*, 2021, **9**, 781779.
27 C. T. G. Retnam, S. V. Rose and B. S. Kumari, *J. Mol. Struct.*, 2023, **1282**, 135162.
28 L. Dkhar, A. K. Verma, V. Banothu, W. Kaminsky and M. R. Kollipara, *Appl. Organomet. Chem.*, 2022, **36**, e6589.
29 S. A. Elsayed, H. M. El-Gharabawy, I. S. Butler and F. M. Atlam, *Appl. Organomet. Chem.*, 2020, **34**, e5643.
30 S. A. Aboafia, S. A. Elsayed, A. K. El-Sayed and A. M. El-Hendawy, *J. Mol. Struct.*, 2018, **1158**, 39–50.
31 S. A. Elsayed, I. M. Elnabky, A. di Biase and A. M. El-Hendawy, *Appl. Organomet. Chem.*, 2022, **36**, e6481.
32 M. M. Aboelnga, *RSC Adv.*, 2022, **12**, 15543–15554.
33 M. M. Aboelnga and S. Kalyaanamoorthy, *ACS Sustainable Chem. Eng.*, 2022, **48**, 15857–15868.
34 R. Kaur, M. M. Aboelnga, D. J. Nikkel and S. D. Wetmore, *Phys. Chem. Chem. Phys.*, 2022, **24**, 29130–29140.
35 M. M. Aboelnga and J. W. Gauld, *J. Phys. Chem. B*, 2017, **25**, 6163–6174.
36 M. M. Aboelnga, J. J. Hayward and J. W. Gauld, *ACS Catal.*, 2017, **7**, 51805193.
37 S. Forli, R. Huey, M. Pique, *et al.*, *Nat. Protoc.*, 2016, **11**, 905–919.
38 G. M. Morris, R. Huey, W. Lindstrom, M. F. Sanner, R. K. Belew, D. S. Goodsell and A. J. Olson, *J. Comput. Chem.*, 2009, **16**, 2785–2791.
39 S. D. Rossella Castagna, P. Colnago, A. Serafini, E. Parisini and C. Bertarelli, *ACS Omega*, 2019, **8**, 13270–13278.
40 T. D. Goddard, E. F. Pettersen, C. C. Huang, G. S. Couch, D. M. Greenblatt, E. C. Meng and T. E. Ferrin, *J. Comput. Chem.*, 2004, **25**(13), 1605–1612.
41 A. Hussain, M. F. AlAjmi, M. T. Rehman, S. Amir, F. M. Husain, A. Alsalme, M. A. Siddiqui, A. A. AlKhedhairy and R. A. Khan, *Sci. Rep.*, 2019, **9**, 1–17.
42 M. Carcelli, P. Cozzini, T. Maccagni, C. Pelizzi and L. Righi, *Inorg. Chim. Acta*, 2000, **303**, 238–243.
43 F. Hueso-Ureña, N. A. Illán-Cabeza, M. N. Moreno-Carretero, A. L. Peñas-Chamorro and R. Faure, *Polyhedron*, 2000, **19**, 689–693.
44 F. B. Tamboura, P. M. Haba, M. Gaye, A. S. Sall, A. H. Barry and T. Jouini, *Polyhedron*, 2004, **23**, 1191–1197.
45 R. S. Hunoor, B. R. Patil, D. S. Badiger, R. S. Vadavi, K. B. Gudasi, V. M. Chandrashekhar and I. S. Muchchandi, *Spectrochim. Acta, Part A*, 2010, **77**, 838–844.
46 R. C. Maurya and S. Rajput, *J. Mol. Struct.*, 2007, **833**, 133–144.
47 K. Nakamoto, *Infrared and Raman Spectra of Inorganic and Coordination Compounds, Part B, Applications in Coordination, Organometallic, and BioInorg. Chem.*, John Wiley & Sons, Inc., 6th edn, 2009.
48 M. Ghorbanloo, R. Bikas and G. Małecki, *Inorg. Chim. Acta*, 2016, **445**, 8–16.
49 V. Kamat, A. Kotian, A. Nevrekar, K. Naik, D. Kokare and V. K. Revankar, *Inorg. Chim. Acta*, 2017, **466**, 625–631.
50 G. S. Kurdekar, S. M. Puttanagouda, N. V. Kulkarni, S. Budagumpi and V. K. Revankar, *Med. Chem. Res.*, 2011, **20**, 421–429.
51 R. S. Hunoor, B. R. Patil, D. S. Badiger, R. S. Vadavi, K. B. Gudasi, V. Chandrashekhar and I. Muchchandi, *Spectrochim. Acta, Part A*, 2010, **77**, 838–844.
52 I. L. Paiva, G. S. G. de Carvalho, A. D. da Silva, P. P. Corbi, F. R. G. Bergamini, A. L. B. Formiga, R. Diniz, W. R. do Carmo, C. Q. F. Leite, F. R. Pavan and A. Cuin, *Polyhedron*, 2013, **62**, 104–109.
53 L. M. Fostiak, I. García, J. K. Swearingen, E. Bermejo, A. Castiñeiras and D. X. West, *Polyhedron*, 2003, **22**, 83–92.
54 N. K. Ngan, K. M. Lo and C. S. R. Wong, *Polyhedron*, 2012, **33**, 235–251.
55 S. A. Elsayed, E. E. Saleh, M. M. Aboelnga and E. A. Toson, *J. Inorg. Biochem.*, 2023, **241**, 112132.

56 A. M. Ismail, S. A. El Sayed, I. S. Butler and S. I. Mostafa, *J. Mol. Struct.*, 2020, **1200**, 127088.
57 M. Muralisankar, J. Haribabu, N. S. Bhuvanesh, R. Karvembu and A. Sreekanth, *Inorg. Chim. Acta*, 2016, **449**, 82–95.
58 G. Ayyannan, M. Mohanraj, M. Gopiraman, R. Uthayamalar, G. Raja, N. Bhuvanesh, R. Nandhakumar and C. Jayabalakrishnan, *Inorg. Chim. Acta*, 2020, 119868.
59 V. Censi, A. B. Caballero, M. Perez-Hernandez, V. Soto-Cerrato, L. Korrodi-Gregorio, R. Perez-Tomas, M. M. Dell'Anna, P. Mastrorilli and P. Gamez, *J. Inorg. Biochem.*, 2019, **198**, 110749.
60 S. Delaney, M. Pascaly, P. K. Bhattacharya, K. Han and J. K. Barton, *Inorg. Chem.*, 2002, **41**, 1966–1974.
61 K. L. Bergeron, E. L. Murphy, O. Majofodun, L. D. Muñoz, J. C. Williams and K. H. Almeida, *Mutat. Res. Genet. Toxicol. Environ. Mutagen*, 2009, **673**, 141–148.
62 K. Sudeepa, N. Narsimha, B. Aparna, S. Sreekanth, A. V. Aparna, M. Ravi, J. Mohmed and C. S. Devi, *J. Chem. Sci.*, 2018, **130**, 52.
63 Y. Jung and S. J. Lippard, *Chem. Rev.*, 2007, **107**, 1387–1407.
64 H.-K. Liu and P. J. Sadler, *Acc. Chem. Res.*, 2011, **44**, 349–359.
65 E. Movahedi, A. R. Rezvani and H. Razmazma, *Int. J. Biol. Macromol.*, 2019, **126**, 1244–1254.
66 A. Wolfe, G. H. Shimer Jr and T. Meehan, *Biochemistry*, 1987, **26**, 6392–6396.
67 Y. Sun, S. Bi, D. Song, C. Qiao, D. Mu and H. Zhang, *Sens. Actuators, B*, 2008, **129**, 799–810.
68 M. V. Babak, S. M. Meier, A. A. Legin, M. S. Adib Razavi, A. Roller, M. A. Jakupec, B. K. Keppler and C. G. Hartinger, *Chem.–Eur. J.*, 2013, **19**, 4308–4318.
69 V. D. Suryawanshi, L. S. Walekar, A. H. Gore, P. V. Anbhule and G. B. Kolekar, *J. Biol. Chem.*, 2016, **6**, 56–63.
70 S. Kathiresan, S. Mugesh, M. Murugan, F. Ahamed and J. Annaraj, *RSC Adv.*, 2016, **6**, 1810–1825.
71 M. Idowu, E. Lamprecht and T. Nyokong, *J. Photochem. Photobiol. Chem.*, 2008, **198**, 7–12.
72 K. Sakthikumar, R. V. Solomon and J. D. Raja, *RSC Adv.*, 2019, **9**, 14220–14241.
73 M. Anjomshoa, S. J. Fatemi, M. Torkzadeh-Mahani and H. Hadadzadeh, *Spectrochim. Acta, Part A*, 2014, **127**, 511–520.
74 D. Xu, X. Wang, D. Fei and L. Ding, *Nucleos Nucleot.*, 2010, **29**, 854–866.
75 A. Ray, B. K. Seth, U. Pal and S. Basu, *Spectrochim. Acta, Part A*, 2012, **92**, 164–174.
76 J. Toneatto and G. A. Argüello, *J. Inorg. Biochem.*, 2011, **105**, 645–651.
77 M. H. Chowdhury, K. Aslan, S. N. Malyn, J. R. Lakowicz and C. D. Geddes, *J. Fluoresc.*, 2006, **16**, 295–299.
78 J. R. Lakowicz, *Principles of Fluorescence Spectroscopy*, Springer science & business media, 2013.
79 J. R. Lakowicz and G. Weber, *Biochem.*, 1973, **12**, 4161–4170.
80 W. R. Ware, *J. Phys. Chem.*, 1962, **66**, 455–458.
81 X. Zhang, S. Li, L. Yang and C. Fan, *Spectrochim. Acta, Part A*, 2007, **68**, 763–770.
82 E. Froehlich, J. Mandeville, C. Jennings, R. Sedaghat-Herati and H. Tajmir-Riahi, *J. Phys. Chem. B*, 2009, **113**, 6986–6993.
83 N. Wang, L. Ye, F. Yan and R. Xu, *Int. J. Pharm.*, 2008, **351**, 55–60.
84 R. A. Khan, I. I. BinSharfan, S. S. Alterary, H. Alsaeedi, F. A. Qais, A. AlFawaz, A. D. Hadi and A. Alsalme, *Appl. Organomet. Chem.*, 2022, **36**, e6550.
85 P. Wiji Prasetyaningrum, A. Bahtiar and H. Hayun, *Sci. Pharm.*, 2018, **86**, 25.
86 S. A. Elsayed, H. E. Badr, A. di Biase and A. M. El-Hendawy, *J. Inorg. Biochem.*, 2021, **223**, 111549.
87 S. Roy, S. Saha, R. Majumdar, R. R. Dighe and A. R. Chakravarty, *Polyhedron*, 2010, **29**, 3251–3256.
88 D. A. Guk, O. O. Krasnovskaya and E. K. Beloglazkina, *Russ. Chem. Rev.*, 2021, **90**, 1566.
89 H. Y. Khan, M. O. Ansari, G. Shadab, S. Tabassum and F. Arjmand, *Bioorg. Chem.*, 2019, **88**, 102963.
90 M. Marloye, G. Berger, M. Gelbcke and F. Dufrasne, *Future Med. Chem.*, 2016, **8**, 2263–2286.
91 Y. Wang, J. Hu, Y. Cai, S. Xu, B. Weng, K. Peng, X. Wei, T. Wei, H. Zhou, X. Li and G. Liang, *J. Med. Chem.*, 2013, **56**, 9601–9611.
92 K. A. Abu-Safieh, A. S. Abu-Surrah, H. D. Tabba, H. A. AlMasri, R. M. Bawadi, F. M. Boudjelal and L. H. Tahtamouni, *J. Chem.*, 2016, **2016**, 508724.
93 S. D. Brown, K. D. Trotter, O. B. Sutcliffe, J. A. Plumb, B. Waddell, N. E. B. Briggs and N. J. Wheate, *Dalton Trans.*, 2012, **41**, 11330–11339.
94 S. K. Liew, S. Malagobadan, N. M. Arshad and N. H. Nagoor, *Biomolecules*, 2020, **10**, 138.
95 C.-R. Sihn, E.-J. Suh, K.-H. Lee, T.-Y. Kim and S. H. Kim, *Cancer Lett.*, 2003, **201**, 203–210.
96 I. Vermes, C. Haanen and C. Reutelingsperger, *J. Immunol. Methods*, 2000, **243**, 167–190.